Direct measurement of neon production rates by (α,n) reactions in minerals

Stephen E. Cox [a,*], Kenneth A. Farley [a], Daniele J. Cherniak [b]

[a] *Division of Geological and Planetary Sciences, California Institute of Technology, Pasadena, CA 91125, USA*
[b] *Department of Earth and Environmental Sciences, Rensselaer Polytechnic Institute, Troy, NY 12180, USA*

Abstract

The production of nucleogenic neon from alpha particle capture by ^{18}O and ^{19}F offers a potential chronometer sensitive to temperatures higher than the more widely used (U–Th)/He chronometer. The accuracy depends on the cross sections and the calculated stopping power for alpha particles in the mineral being studied. Published $^{18}O(\alpha,n)^{21}Ne$ production rates are in poor agreement and were calculated from contradictory cross sections, and therefore demand experimental verification. Similarly, the stopping powers for alpha particles are calculated from SRIM (Stopping Range of Ions in Matter software) based on a limited experimental dataset. To address these issues we used a particle accelerator to implant alpha particles at precisely known energies into slabs of synthetic quartz (SiO_2) and barium tungstate ($BaWO_4$) to measure ^{21}Ne production from capture by ^{18}O. Within experimental uncertainties the observed ^{21}Ne production rates compare favorably to our predictions using published cross sections and stopping powers, indicating that ages calculated using these quantities are accurate at the ~3% level. In addition, we measured the $^{22}Ne/^{21}Ne$ ratio and (U–Th)/He and (U–Th)/Ne ages of Durango fluorapatite, which is an important model system for this work because it contains both oxygen and fluorine. Finally, we present $^{21}Ne/^4He$ production rate ratios for a variety of minerals of geochemical interest along with software for calculating neon production rates and (U–Th)/Ne ages.
© 2014 Elsevier Ltd. All rights reserved.

1. INTRODUCTION

Alpha particles produced by the decay of uranium and thorium series nuclides interact with light elements in minerals to produce the three stable isotopes of neon. Nuclides created by such secondary nuclear reactions are termed nucleogenic, and can be produced by alpha particle capture and also by capture of neutrons emitted by alpha particle capture. Wetherill (1954) was the first to recognize production of nucleogenic neon, from (α,n), (α,p), and (n,α) reactions in minerals containing uranium and thorium. Neon produced by these reactions is also readily apparent in crustal well gases (Kennedy et al., 1990). Yatsevich and Honda (1997), who were primarily interested in the neon budget of Earth's mantle and atmosphere, proposed the use of nucleogenic neon as a chronometer. They established that the reaction $^{18}O(\alpha,n)^{21}Ne$ dominates the nucleogenic production of neon in crust and mantle, and that the reaction $^{24}Mg(n,\alpha)^{21}Ne$ is insignificant in comparison. In addition, using published neutron capture cross section measurements they arrived at a mean bulk crustal production rate ratio $^{21}Ne/^4He = 4.5 \times 10^{-8}$, which is consistent with current estimates and measurements for U- and Th-bearing minerals, yet is much higher than earlier estimates (Kyser and Rison, 1982). Using similar data, Leya and Wieler (1999) calculated the production rate of ^{21}Ne and ^{22}Ne in specific minerals of geochemical interest, such as apatite and zircon. Gautheron et al. (2006) modeled the production

rate of $^{18}O(\alpha,n)^{21}Ne$ on the basis of a different analysis of the published cross section data and arrived at production rates that differed by up to ∼10% from those of Leya and Wieler (1999). They also presented (U–Th)/Ne age determinations on several apatite and zircon samples using these production rates and considered the consequences for dating of the spatial separation of parent nuclides from both helium and neon daughter products due to alpha ejection and the energy-dependence of the neon production rate.

The (U–Th)/Ne geochronometer is potentially useful in rapidly cooled samples and as a chronometer of the minimum age of mineral formation. In the former case, one simply assumes that the rock cooled so quickly that diffusive loss of neon has been negligible for its entire history, and in the latter case, one acknowledges that diffusive loss may have occurred and accounts for this possibility in the geologic interpretation. For example, Farley and Flowers (2012) applied (U–Th)/Ne dates as a minimum age for the formation of a hematite specimen from the Grand Canyon.

As discussed by Gautheron et al. (2006), (U–Th)/Ne ages can also be used for thermochronometry. Ideally a thorough understanding of the temperature dependence of neon diffusion supports such an application. However, because laboratory diffusivity measurements are usually made under environmental conditions (temperature, pressure, chemical activity) much different from the natural setting, care is required in interpreting the laboratory data. This is especially true for some phases of interest for (U–Th)/Ne dating, such as apatite, because phase modification via volatile loss in a high temperature vacuum chamber is possible (Nadeau et al., 1999). As an alternative approach, approximate closure temperatures for neon can be obtained by comparison of neon ages to those of other thermochronometers in the same rock (Gautheron et al., 2006).

1.1. The production of neon by uranium and thorium decay

In the (U–Th)/He system, multiple parents (uranium-238, uranium-235, and thorium-232) decay through chains in which they emit a series of alpha particles with discrete energies. Samarium-147 is also an alpha emitter, but because it produces just one alpha particle and because of its very low energy, this nuclide contributes little to nucleogenic production. The vast majority of alpha particles come to rest as ^{4}He atoms, but a small number (fewer than one in ten million) react with other elements in a mineral to form nuclear reaction products. A particularly important reaction is $^{18}O(\alpha,n)^{21}Ne$, which produces measurable neon in many oxide and silicate minerals (Yatsevich and Honda, 1997; Leya and Wieler, 1999; Gautheron et al., 2006; Farley and Flowers, 2012). The reaction $^{19}F(\alpha,n)^{22}Ne$ is even more productive per alpha particle, but is important only in minerals that contain significant fluorine, such as apatite, titanite, or fluorite (Solé and Pi, 2006). Although only limited data exist, all analyzed minerals are more retentive of neon than of helium (Shuster and Farley, 2005; Tournour and Shelby, 2008a,b; Behrens, 2010; Cherniak et al., 2014). This suggests the possibility of using measured neon concentrations in minerals as a chronometer like (U–Th)/He, but retentive to higher temperatures

(Yatsevich and Honda, 1997; Leya and Wieler, 1999; Gautheron et al., 2006). However, a known rate of neon production is critical for any chronometric application, and existing estimates based on neutron production measurements are not in sufficient agreement for high-precision geochronology (Leya and Wieler, 1999; Gautheron et al., 2006). In this paper we take a different approach than previous workers to establishing ^{21}Ne production rates. We measure the neon itself in target phases exposed to energetic alpha particles of precisely known energy. This work is analogous to the oxygen gas target experiments of Hünemohr (1989) but undertaken on solid phases. We also present new high precision U–Th–He–Ne data on Durango apatite, which confirm the validity of our ^{21}Ne results in a natural system and also provide a production rate estimate for the ^{22}Ne reaction from alpha capture by ^{19}F.

For (U–Th)/Ne chronometry, we are primarily interested in the two reactions $^{18}O(\alpha,n)^{21}Ne$ and $^{19}F(\alpha,n)^{22}Na(\beta^+)^{22}Ne$ (simplified as $^{19}F(\alpha,n)^{22}Ne$ hereafter due to the insignificance of the 2.6 year ^{22}Na decay over geologic time). These reactions occur at a rate proportional to the number of alpha particles emitted and to the concentration of the target nuclide (^{18}O or ^{19}F) in the mineral. Furthermore, the rate of these reactions also depends on the cross section of the target nuclide for alpha particles and the chemical composition of the host mineral. Below, we describe the physical controls on this reaction and how they are measured or calculated in order to arrive at a nucleogenic neon production rate.

Neon isotope production from (n,α) reactions on Mg can be safely ignored for minerals that do not contain large amounts (wt%) of Mg. For example, O is about three times as productive of neon as Mg, so these production pathways only become significant at the 1% level for Mg/O > 0.03 (in the case of ^{21}Ne). Magnesium is even less productive of neon than F, so these production pathways become significant at the 1% level for Mg/F > 0.07 (in the case of ^{22}Ne). In minerals that include magnesium as a stoichiometric constituent, these reactions must be considered in the neon budget.

The rate of a given nuclear reaction depends on the nuclear properties of the target nuclide and the energy of the incident particle, and is characterized by the nuclear cross section parameter ($\sigma(E)$). The cross section is an areal representation of the probability of reaction in a pure sample of the target nuclide and is frequently described in units of millibarns (1 barn = 10^{-24} cm^2). A larger cross section means that the reaction is proportionally more likely to occur when a single particle interacts with the target, or proportionally more frequent when a large number of particles interact with the target. Over the energy range of interest here, cross sections for neon-producing alpha particle reactions generally increase with alpha energy. Cross sections for neon producing reactions have been measured over the last several decades (Bair and Willard, 1962; Hansen et al., 1967; Bair and Del Campo, 1979; Norman et al., 1984), usually using a thin-target approach in which the cross section is determined by measuring the production rate of neutrons using alpha particles at just a single energy. In contrast, nucleogenic neon production in a mineral

involves reactions occurring along the entire trajectory as the alpha particle slows and eventually comes to rest, and thus involves an integral along the alpha particle energy path. These observations have three important implications: neon production will be higher for alpha particle decays with high characteristic energy; neon production will depend on how fast alpha particles lose energy within a given mineral; and neon production will preferentially occur early in the alpha particle trajectory, where energies are highest.

Stopping power S(E) describes the rate of energy loss of a given particle as it travels through a given material. Stopping power depends on the interactions of incident particles with both the nuclei and electron clouds of the atoms in the host mineral. In practice the electronic stopping power is several orders of magnitude larger than the nuclear stopping power and dominates at energies of interest here. Relativistic effects can be ignored here because alpha particles produced by radioactive decay are well below the energy at which such effects become significant (about 35 MeV). Stopping power is represented with density-normalized units of $MeV/(mg/cm^2)$ to avoid the requirement of measuring density in natural samples. Like the cross section, stopping power is dependent on the energy of the incident alpha particles, so it must also be considered as an integral quantity as these particles lose energy and come to rest. Many studies have measured and modeled stopping powers in great detail (e.g., SRIM and references therein; Ziegler et al., 2010).

Reaction cross section, oxygen-18 or fluorine-19 content, and stopping power of a given mineral are the basic ingredients required to predict the neon production rate from alpha-emitting radionuclides. Production is linearly proportional to the concentration of the target nuclide in the host mineral, and is proportional to an energy-dependent integral quantity that includes both the cross section and the total stopping power for alpha particles in the host mineral. We will take this integral from rest ($E_\alpha = 0$ MeV) to the energy of each alpha particle emitted during alpha decay. As an example, in the next section we construct the yield equation for ^{21}Ne from ^{18}O for a given alpha particle in a generic mineral Z.

We represent the concentration of ^{18}O in Z as the product of the mass fraction of oxygen (X_O) in the mineral and the isotopic abundance of ^{18}O (N_{18}/N_O), divided by the total atomic mass of one formula unit of the mineral (A_Z). We multiply this quantity by the Avogadro constant (N_A) to arrive at $(X_O)(N_{18}/N_O)(N_A/A_Z)$, which has units of atoms/gram.

'The integral quantity that describes the rate of reaction as an alpha particle interacts with the target mineral scales with the cross section (a higher cross section means more production) and scales inversely with stopping power (a higher rate of energy loss means less neon production). As a consequence our integrand is the cross section $\sigma(E)$ divided by the mineral-dependent stopping power $S_Z(E)$. We then integrate this from rest ($E_\alpha = 0$ MeV) to the energy of the incident alpha particle $E_{\alpha k}$. We arrive at the term, $\int_0^{E_{\alpha k}} \frac{\sigma(E)}{S_Z(E)} dE$ which has units of (mbarn)(mg/cm²).

Finally, we multiply by 10^{-3} to convert mbarn to barn, 10^{-24} to convert barn to cm², and 10^{-3} again to convert mg to g, which allows us to arrive at the following complete yield equation (e.g., Yatsevich and Honda)

$$Y_{21_{Ne}} = 10^{-30} \frac{N_A}{A_Z} X_O \frac{N_{18}}{N_0} \int_0^{E_{\alpha k}} \frac{\sigma(E)}{S_Z(E)} dE \quad (1)$$

This equation has units of atoms and reflects the production rate of neon for a single alpha particle k of initial energy $E_{\alpha k}$. This quantity will be quite small, about 5×10^{-8}, because most alpha particles come to rest as ^{4}He without reaction.

As a concrete example, we illustrate this calculation for quartz (SiO_2) and barium tungstate ($BaWO_4$) in Fig. 1. Fig. 1a shows the cross section for the reaction $^{18}O(\alpha,n)^{21}$Ne as a function of alpha particle energy, with original data points in black circles and the smoothed interpolation presented as a red line (Section 1.2), Fig. 1b shows the stopping power for alpha particles in quartz as a function of alpha particle energy (Ziegler et al., 2010), Fig. 1c shows the integrand $\frac{\sigma(E)}{S_Z(E)}$ as a function of alpha particle energy, and Fig. 1d shows the full yield equation given stoichiometric $X_O = 0.5326$ and $\delta^{18}O_{VSMOW} = +2$ ($^{18}O/O = 0.002005$).

The yield equation for ^{21}Ne from alpha particles in quartz (Fig. 1d) demonstrates several notable features. The production rate increases toward the higher energy end of the alpha energies produced by uranium and thorium decay, so these decays will dominate the total nucleogenic neon in a sample. Conversely, alpha emitters with no high-energy decays (^{147}Sm, for example) will produce negligible nucleogenic neon. In addition, because alpha particles are more productive when first emitted (at their highest energy), most nucleogenic neon will be produced closer to the alpha emitter than the final rest position of ^{4}He that does not react. This means that the alpha ejection correction for neon produced by alpha particles will be smaller than the alpha ejection correction for radiogenic helium in the same minerals (Gautheron et al., 2006).

1.2. Physical quantities used to predict neon production rates

For use in chronometry it is both impractical and unnecessary to measure neon production rates at many alpha energies for a large number of minerals. One may instead use a (validated) cross section and stopping powers calculated from SRIM, along with the stoichiometric oxygen concentrations and assumed or measured oxygen isotopic compositions of any mineral to calculate a neon production rate. In this section we predict ^{21}Ne production rates in synthetic materials using these methods, and then compare the prediction to our measured production rates in order to validate the cross sections and stopping powers. We chose the minerals quartz (SiO_2) and barium tungstate ($BaWO_4$) because we were able to obtain large, optically pure synthetic crystals of each and because the stopping power for alpha particles in quartz is almost twice as high as in barium tungstate, so we can easily deconvolve the effects of cross section and stopping power on the measured neon production rates.
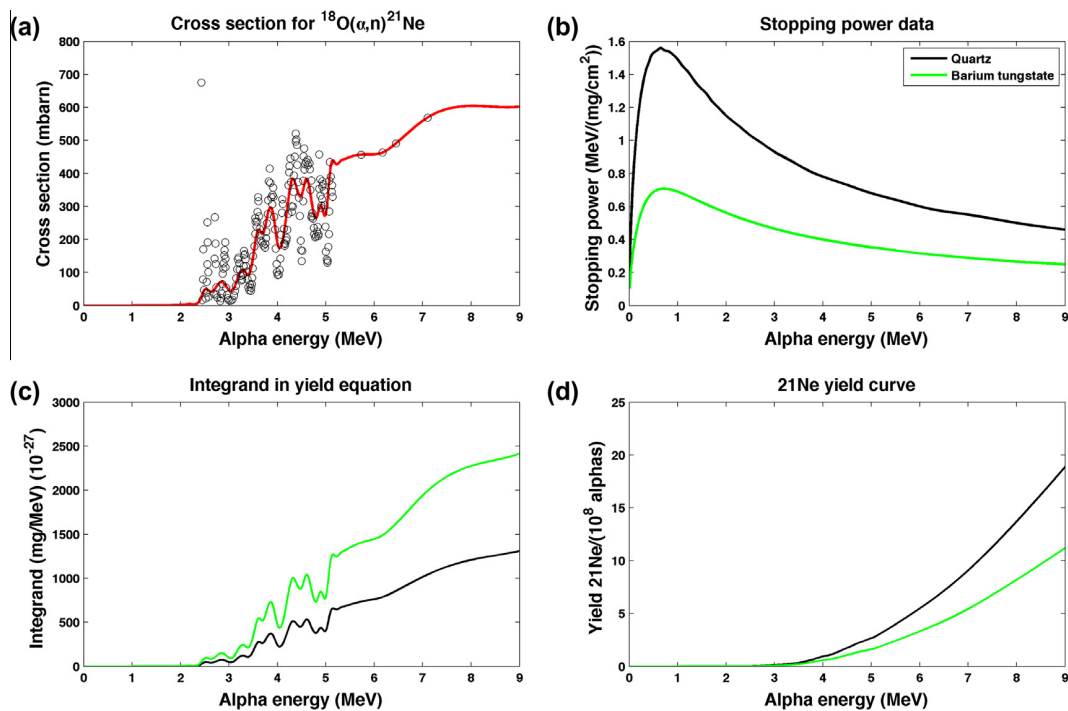
Fig. 1. An illustration of the steps involved in calculating ^{21}Ne yield from alpha particles in quartz (SiO2; black) and barium tungstate (BaWO4; green). The figure shows (a) the interpolated cross section of the reaction ^{18}O(α,n)^{21}Ne, including the renormalized (Bair and Del Campo, 1979) data of Bair and Willard (1962) and the high energy data of Hansen et al. (1967), (b) the density-normalized stopping power for alpha particles in quartz and barium tungstate, (c) the integrand $\sigma(E)/S_Z(E)$ from the yield equations, and (d) the calculated yield for ^{21}Ne from alpha particles in quartz and barium tungstate. (For interpretation of the references to colour in this figure legend, the reader is referred to the web version of this article.)

The concentration of ^{18}O in a mineral exhibits linear control on the production rate of neon in the reaction ^{18}O(α,n)^{21}Ne, so it is crucial to account for stoichiometric variations in oxygen composition and to note the oxygen concentration used in calculating reported (U–Th)/Ne ages. In the case of measured differences in δ^{18}O or small variations in oxygen concentration, the production rates provided here may be scaled linearly because the changes in alpha particle stopping powers will be small. The mass fraction of oxygen in mineral phases is usually known from stoichiometry, and the variations in oxygen isotopic composition measured in natural minerals are usually small compared to other uncertainties in the (U–Th)/Ne system. We measured δ^{18}O = +25‰ for our synthetic barium tungstate and δ^{18}O = 0‰ for our synthetic quartz using the laser fluorination method at Caltech (Eiler et al., 2000). We assume a common igneous δ^{18}O$_{VSMOW}$ = +6‰ (^{18}O/O = 0.002012) for the other calculations presented here unless otherwise noted. The user may modify this value in the software provided in the appendix.

The ^{18}O(α,n)^{21}Ne cross section used by (Gautheron et al., 2006) is based on a critically evaluated compilation of data from several sources and includes numerous resolved resonances. The thin target experiments vary in quality and include a dataset from Bair and Willard (1962) that was later renormalized by a factor of 1.35 by (Bair and Del Campo, 1979) because the original thin target thicknesses were measured incorrectly. Following Gautheron et al. (2006), for our predicted ^{21}Ne yields we use a 0.01 MeV interpolation of the renormalized Bair and Willard (1962) data below 5.14 MeV because it is the most detailed, and we supplement it with the more sparse data from Hansen et al. (1967) in the energy range above 5.14 MeV (Fig. 1a).

We also adopt the cross section curve for the ^{19}F(α,n)^{22}Ne reaction presented by Murata et al. (2006), which is based on a small amount of very sparse experimental thin target data. As noted by Murata et al. (2006), numerous resonances were observed in this reaction below alpha energies of 3.1 MeV by Wrean and Kavanagh (2000). Although these resonances are too low energy to be important for neon production, similar features must exist in the energy range of interest (primarily 3–8 MeV, because alpha particles with higher energy are not emitted by uranium and thorium series decay, and alpha particles with lower energy produce very little neon; Fig. 1) for (U–Th)/Ne dating as well, but have not been documented. Thus the ^{19}F(α,n)^{22}Ne cross section should be used with more caution than the cross section for the reaction ^{18}O(α,n)^{21}Ne owing to the sparseness of these measurements.

We computed the stopping powers of the minerals of interest using SRIM (Ziegler et al., 2010) with stoichiometries found on webmineral.com. The primary limitations of SRIM are that it depends on experimental data that can vary in quality and that it does not account for crystal structure but rather assumes an amorphous phase.

However, experimental data for alpha particles are relatively plentiful, and the stopping of ions is dominated by electronic collisions that will not be greatly affected by crystal structure. Effects such as channeling in a crystal lattice can be neglected due to very low probability and low impact on total neon production. While we suspect errors introduced to our calculations from the stopping powers from SRIM are small, our experimental measurements, involving phases with very different predicted stopping powers, allow us to assess this expectation.

The calculated neon production rates for other minerals allow users to calculate (U–Th)/Ne ages from uranium, thorium and neon data for a wide variety of minerals of geochemical interest (Section 4.3). As explained above, oxygen concentration and stopping power both affect the production rate of nucleogenic neon in a given mineral, so the differences between minerals include both of these effects.

1.3. Neon-21 production rates measured by alpha particle implantation

As mentioned above, previously published ^{21}Ne production rates estimated for uranium- and thorium-containing minerals differ by up to ~10% (Leya and Wieler, 1999; Gautheron et al., 2006), which is greater than the uncertainty of most noble gas measurements. This discrepancy is sufficiently large as to preclude accurate chronometry and is primarily related to different interpretations of sparse and contradictory ^{18}O(α,n)^{21}Ne cross section data (Bair and Willard, 1962; Hansen et al., 1967; Bair and Del Campo, 1979). Note that our calculations in Section 1.1 use the same approach for establishing the ^{18}O(α,n)^{21}Ne cross section as Gautheron et al. (2006), so are not an independent estimate for comparison.

To assess the accuracy of the predicted ^{21}Ne production rates, we directly measured the rates by implanting a known fluence of alpha particles of a single energy into thick targets (i.e., mineral samples in which all alpha particles stop) of synthetic materials and then measuring the amount of ^{21}Ne produced.

While quartz and barium tungstate are not likely to be targets of (U–Th)/Ne chronometry, they were appealing choices for several reasons. As noted above, their extreme contrast in stopping power may allow us to distinguish errors in stopping power from errors in cross section. In addition, we were able to obtain large optical grade crystals in both cases, which ensured homogenous samples of adequate size for the experiment. We experimentally verified that the samples were free of neon and helium before performing the implantations. Measured quantities are exclusively a product of the implantation experiment.

1.4. A natural test of the ^{21}Ne production rate and preliminary ^{22}Ne production rate from Durango apatite

Fluorine is a challenging target for (U–Th)/Ne chronometry as it substitutes readily for hydroxyl and chlorine in many minerals and is therefore often not stoichiometric. In addition, it is more difficult to measure accurately than oxygen, e.g., by electron probe. However, the target nuclide ^{19}F is the only isotope in natural fluorine, and the cross section of neon production from ^{19}F is higher than for ^{18}O. Using Durango fluorapatite as a model system, we explored the potential use of ^{22}Ne produced by ^{19}F as an independent chronometer and as a counterpart to ^{21}Ne produced by ^{18}O in the same phase. Even with a less well-known production rate, ^{22}Ne is potentially useful as a relative chronometer (Solé and Pi, 2006) or as a target for diffusivity studies in fluorine-rich minerals, and is useful for deducing the presence of a fluorine-bearing phase (e.g., an inclusion) in a studied sample.

1.5. Samarium-147 and cosmogenic neon

We do not consider the impact of ^{147}Sm or of cosmogenic neon production in the calculations in this paper. These are irrelevant for our synthetic samples, in which we control the sole production pathway for neon, but they might be relevant in Durango fluorapatite and other natural minerals that contain significant rare earth elements and/or that have been exposed to cosmic radiation. However, ^{147}Sm emits a single alpha particle with energy of only 2.23 MeV. The neon production rate at this energy is negligible due to the extremely low cross section for the reactions ^{18}O(α,n)^{21}Ne and ^{19}F(α,n)^{22}Ne in this energy range (Fig. 1; Wrean and Kavanagh, 2000).

Cosmogenic neon dating has applications to many surface processes, especially to ancient surfaces that cannot be dated as effectively using radioactive nuclides such as ^{10}Be. Durango fluorapatite is mined from below the surface so should be free of this component, but cosmogenic neon is a potential contaminant for samples that have been exposed within ~1 m of Earth's surface for a substantial period of time, so it should be considered during sampling and in cases for which the rock history is unknown. Production rates of cosmogenic neon are mineral-dependent, but are typically of the order of a few tens of atoms per gram per year. Cosmogenic neon is produced with a distinctive isotope ratio (mineral-dependent, but roughly subequal in all three isotopes; Niedermann, 2002) compared to air and nucleogenic neon, so one can usually recognize it by analyzing all three neon isotopes. When helium is also analyzed, the presence of ^{3}He can be an indicator of cosmogenic nuclide contamination.

2. EXPERIMENTAL

2.1. Sample selection and preparation

We prepared ~1 cm square and ~1 mm-thick slabs of quartz and barium tungstate by cutting with a wire saw and cleaning in an ultrasonic bath of 18.2 MΩ purified water to ensure that no residue from the cutting slurry was present. These samples are far thicker than the average stopping distance for alpha particles in either mineral (~15–30 μm depending on energy) and therefore represent thick targets that effectively stop all incident alpha particles.

The quartz and barium tungstate analyzed in this study had low concentrations of non-nucleogenic (air-like) neon, with nucleogenic neon typically representing >85% of the

measured ^{21}Ne. In minerals that tend to release more air neon, such as hematite (Farley and Flowers, 2012), the uncertainty is often limited by the correction for air contamination, which effectively raises the background level against which the nucleogenic neon signal must be resolved. Finally, the presence of non-atmospheric neon from mantle or crustal fluid sources could complicate nucleogenic neon measurements, and should be considered in the case of measured isotope ratios that do not fall on an air-nucleogenic mixing line.

We prepared the Durango fluorapatite samples from crushed and homogenized aliquots of a single gem-quality crystal such as the ones used for (U-Th)/He development (Farley, 2000). The crushing and homogenization procedure ensures that the uranium, thorium, neon, and helium distributions are homogenous between samples even though the large crystal may have uranium and thorium zonation as reported by Boyce and Hodges (2005).

2.2. Alpha particle implantation

We implanted alpha particles using the 4 MV Dynamitron linear accelerator at SUNY-Albany. In order to produce alpha particles with energies in the range of approximately 4–8 MeV, which is the range encountered in the decay chains of ^{238}U, ^{235}U, and ^{232}Th, we used doubly charged particles accelerated at 2–4 MV. Using the calculations described in Section 1, we chose the alpha particle fluence for each energy by calculating the fluence necessary to achieve an easily measurable quantity of neon. The alpha particle fluence we used ranged from $\sim10^{14}$ particles for the highest energy (most productive) experiments to $\sim10^{15}$ particles for the lowest energy experiments.

We identified the helium beam produced by the Dynamitron using the spectra of backscattered particles from a synthetic silica slab, which produce a characteristic spectrum of backscattered alpha particles in measurements with a solid-state surface barrier detector. After focusing the beam, we placed the synthetic target (either quartz or barium tungstate) in the path of the incident beam and then measured accumulated charge in order to achieve the desired alpha particle fluence. Spectra of backscattered particles from each sample during the implantations were also monitored and collected with a solid-state surface barrier detector to ensure that only an alpha particle beam was implanted into samples during the experiments. We also monitored the shape and position of the incident beam during each experiment to ensure complete collection of beam on the targets. The Dynamitron has an energy resolution ($\Delta E/E$) of about 10^{-4}. The nominal uncertainty of this measurement is quite low (better than 1 ppm), but the practical uncertainty is limited to about 2% by the purity of the helium beam (Section 2.4).

At energies above 7 MeV, we experienced problems with beam stability and associated inadvertent implantation of hydrogen along with the helium beam. This hydrogen does not produce neon, but is included in the integrated beam current measurement along with the helium. During the implantation, a solid-state surface barrier detector set at 167.5 degrees with respect to the incident beam was used to monitor the beam, and assess whether there was any contamination of the incident helium beam by hydrogen. This could be evaluated by observation of changes in the backscatter signal if the spectra included features characteristic of hydrogen backscattered from the elemental constituents of the sample, along with spectra produced by the backscattered helium.

2.3. Neon

2.3.1. Neon mass spectrometry

We measured neon using a GV Helix SFT static vacuum magnetic sector noble gas mass spectrometer with a Balzers SEV-217 ion counting multiplier and a mass resolution (R) of approximately 800 ($m/\Delta m$, Δm = peak width at 5% of maximum peak height). To extract neon from the samples, we first degassed them in a double vacuum furnace at temperatures of 1100–1300 °C, and then removed other gases using non-evaporable getters, a liquid nitrogen cryogenic trap, and a focusing cryostat. We isolated neon on a cryostat at 21 K and then pumped away helium to avoid detrimental effects of many orders of magnitude more helium than neon in the mass spectrometer. Some helium is retained at this nominal temperature on our cryostat, but we observe that the majority is removed. Neon-21 beams were several hundred counts per second (cps), well above multiplier backgrounds of $\sim$0.15 cps and procedural blanks of $\sim$3 cps. We measured each neon isotope beam on the multiplier by peak hopping with the accelerating voltage at a fixed magnetic field to avoid hysteresis effects and settling delays. Between analyses, we measured air standards in the same way as the samples to keep track of mass discrimination and sensitivity in the mass spectrometer. We use isotopic deconvolution and the measured composition of air standards to remove air backgrounds from samples. We are able to pseudo-resolve doubly charged ^{40}Ar from ^{20}Ne ($R = 1777$ for ^{40}Ar^{++} and ^{20}Ne^{+}, $\sim$45% resolved, isobar contribution less than 1‰ at measurement position on ^{20}Ne) adequately enough to measure ^{20}Ne without significant interference when argon concentrations are controlled with the liquid nitrogen cryogenic trap. Doubly-charged carbon dioxide overlaps almost completely with ^{22}Ne ($R = 6229$), but we reduce its small contribution significantly by lowering the electron energy in the ionization source for ^{22}Ne measurement only, which reduces double ionization of carbon dioxide far more than the single ionization of neon. Carbon dioxide backgrounds are stable and less than 5‰ of ^{22}Ne signals, and we remove any carbon dioxide with the two steps of cryogenic separation.

2.3.2. Neon-21 measurement by isotope dilution and sample-standard bracketing

We made ^{21}Ne measurements by isotope dilution using a spike gas artificially enriched in ^{22}Ne relative to air and to the samples to ensure that pumping away the helium does not affect the neon concentration determinations. Our apparatus and spike gas for this application changed over the course of the experiments described here.

The measured isotopic composition of our first spike gas was approximately 8.9% ^{20}Ne, 0.12% ^{21}Ne, and 91% ^{22}Ne.

The improved spike was of >99.5% pure ^{22}Ne. This gas is introduced into the vacuum line just after completion of the neon extraction in the furnace. After spiking, the measured mixture comprises an extraction line background including isobaric interferences, air contamination in the samples and vacuum system, the sample gas, and the spike gas. We measured the spike composition separately and, after subtracting the extraction line background from all other measurements, completely resolve the three components by matrix inversion using the three isotope measurements. The sample concentrations were determined by comparing spiked sample isotope ratios to spiked manometrically calibrated air standards.

The presence of measurable ^{20}Ne and ^{21}Ne in the first spike added to experimental error on both air corrections and ^{21}Ne determinations. In addition, we discovered a problem with the hardware (a virtual leak in the pipette volume) that led to spurious amounts of spike being emitted during a small number of experiments. Fortunately, this problem was easily detected in ^{22}Ne measurements, and could be corrected by using the ^{22}Ne excess to determine how much extra spike we added. However, this method relies on consistent sample-standard measurements and therefore defeats the purpose of using isotope dilution. For this reason, we simply subtract spike and air contamination ^{21}Ne based on the ^{22}Ne and ^{20}Ne measurements for these few samples and present results using conventional sample-standard bracketing to determine absolute abundance. For the vast majority of samples, sample-standard bracketing and isotope dilution yielded statistically indistinguishable results, which confirms that our procedure for pumping away helium does not remove or fractionate neon. In our final results, we report isotope dilution results except when spiking problems suggest the use of the sample-standard bracketing results.

We made the Durango fluorapatite measurements using both sample-standard bracketing and isotope dilution after we redesigned our isotope dilution hardware and spike gas, which allows us to introduce a manometrically calibrated aliquot of the >99.5% pure ^{22}Ne that is repeatable to better than 0.1%. We made the first set of measurements without the addition of spike gas to characterize the isotopic composition of the neon from the fluorapatite, then we made the second set of measurements using the same method as used for the implantation measurements, but we compared the sample concentrations directly to the calibrated spike instead of using sample-standard bracketing.

The analytical uncertainties of neon measurements are about 1.5% (2σ) with isotope dilution, dominated by counting statistics and gas standard calibration, and typically about 2% without isotope dilution. For the two samples that required a significant correction to the sample-standard bracketing result due to the problem with the isotope dilution apparatus, the uncertainty is about 4%. The higher uncertainty of the latter is primarily due to the correction for the added spike, which we calculated using its isotopic composition. We increased the stated uncertainties of these samples to encompass the results from both methods, so some data points have asymmetric uncertainties.

2.4. Helium

For approximately half of the implanted samples we measured for neon, we used the integrated implantation current as the measure of the alpha particle fluence. After it became apparent that two high-energy samples were unusually poor in neon compared to the expected production rate, we began to suspect that hydrogen had been implanted with helium at the highest energies. In addition, in the quartz target at 7.8 MeV, two replicate runs showed evidence of significant hydrogen contamination in the RBS spectra obtained during implantation (see Section 2.2). As a consequence, we then switched to a method that allowed us to split a very small amount of the sample helium and then measure it on a separate mass spectrometer. A split was required because the full sample of implanted helium is several orders of magnitude larger than we can measure. Measuring helium directly allowed us to determine correct neon/helium ratios even in the samples for which the alpha particle beam instability of the Dynamitron resulted in a significant implantation of hydrogen along with the alpha particles.

We isolated 0.18% of each helium sample in a small volume after gas extraction, then analyzed this gas on an MAP 215-50 static vacuum magnetic sector noble gas mass spectrometer connected to the same extraction system as the GV Helix SFT used to measure neon. This split represents an insignificant amount of the neon sample but, due to the $\sim 5 \times 10^{-8}$ production rate ratio of ^{21}Ne to alpha particles, contained enough helium to achieve a signal of tens to hundreds of millivolts on a Faraday cup detector equipped with an amplifier with a 10^{11} ohm resistor. We analyzed gas standards using the same split volume, so that uncertainties in the volume ratio are removed from the calculated helium concentrations. We performed all helium analyses by sample-standard bracketing with a helium-doped air standard developed at Caltech ("Caltech air"). Blank corrections for helium were insignificant.

The uncertainties on helium measurements are about 1%, and are dominated by gas standard calibration. We assigned a 2% uncertainty to helium concentrations calculated from the integrated beam current on the Dynamitron rather than measured directly. The nominal uncertainty of the implantation is far smaller (of order ppm), so this value is somewhat arbitrary and is meant to account for the typical observed scatter between the measured helium concentrations and the integrated beam currents in samples that show no evidence of hydrogen contamination. We assume that this added uncertainty is dominated by small amounts of contamination of the beam with hydrogen, and by measurement uncertainty on the mass spectrometer.

3. RESULTS

3.1. Neon and helium in synthetic targets

Neon and helium measurements and ^{21}Ne/^{4}He ratios in the synthetic quartz and barium tungstate targets are shown in Table 1. Nucleogenic ^{21}Ne/^{4}He ratios are displayed in Fig. 2 for quartz and Fig. 3 for barium tungstate.

Table 1
Neon and helium data for implanted quartz and barium tungstate. Column "Ne Method" indicates whether we used isotope dilution for the neon measurement ("ID") or rejected it due to a hardware problem in favor of sample-standard bracketing ("No ID"). Column "He Method" indicates whether we calculated the amount of implanted helium from the integrated beam current on the Dynamitron with 2% assumed uncertainty ("Current") or from a direct measurement by mass spectrometry ("MS"). Last two columns give the + and − uncertainties separately since they are asymmetric. All uncertainties are 1 standard deviation.

Alpha Energy	Ne method	He method	^{21}Ne (Mat)	^{21}Ne ± (Mat)	^{4}He (Tat)	^{4}He ± (Tat)	^{21}Ne/^{4}He (10^{-8})	^{21}Ne/^{4}He +	^{21}Ne/^{4}He −
Quartz									
4.5	No ID	Current	16.5	1.8	1163	23	1.58	0.08	0.17
5.00	No ID	Current	13.3	1.5	684	14	2.63	0.13	0.68
5.25	ID	Current	14.3	0.6	467	9	3.06	0.12	0.12
5.50	ID	Current	14.0	0.6	397	8	3.51	0.14	0.14
6.00	ID	Current	18.2	0.7	343	7	5.30	0.21	0.21
6.25	ID	Current	18.5	0.8	300	6	6.17	0.25	0.25
6.50	ID	Current	18.4	0.8	264	5	6.96	0.28	0.28
7.00	ID	Current	18.9	0.8	210	4	9.00	0.36	0.36
7.30	ID	Current	16.5	0.7	170	3	9.72	0.39	0.39
7.80	ID	Current	10.4	1.1	140	3	7.47	0.82	0.82
7.80	ID	Current	14.8	0.2	140	3	10.6	0.15	0.15
BaWO$_4$									
4.5	ID	MS	9.09	0.15	892	2	1.02	0.02	0.05
5	ID	MS	12.2	0.2	710	1	1.72	0.03	0.06
5.25	ID	MS	10.9	0.2	570	1	1.92	0.03	0.10
5.5	No ID	MS	8.36	0.13	481.7	1.0	2.43	0.12	0.69
6	ID	MS	11.3	0.2	335.2	0.7	3.38	0.05	0.05
6	ID	MS	10.6	0.2	332.7	0.7	3.18	0.05	0.05
6.25	ID	MS	12.1	0.2	291.8	0.6	4.13	0.07	0.07
6.5	ID	MS	12.9	0.2	293.8	0.6	4.40	0.07	0.07
7	ID	Current	13.4	0.2	250	5	5.35	0.08	0.08
7.3	ID	MS	11.5	0.2	184.4	0.4	6.22	0.10	0.57
7.8	ID	MS	16.5	0.3	209.1	0.4	7.89	0.47	0.12

Fig. 2. Comparison of measured ^{21}Ne yields per alpha particle in quartz with predictions based on the published cross sections of Gautheron et al. (2006) and stopping powers described in Section 1.2. The measured values at 7.8 MeV are internally inconsistent and probably represent uncorrected contamination of the alpha particle beam with hydrogen. Also shown are the relative distributions of alpha particle energies in each of the uranium and thorium decay chains.

The ^{21}Ne concentrations are between 8 and 19 million atoms in each sample. For the samples in which it was directly measured, ^{4}He concentrations range from 140×10^{12} to 1163×10^{12} atoms. With two exceptions, these numbers agreed with the total measured beam current. As expected, in both targets the ^{21}Ne/^{4}He ratios increase monotonically with alpha particle energy. The only exceptions are the two data points at $E_\alpha = 7.8$ MeV in quartz (Fig. 2); these are the samples with a large amount of contamination of the beam with hydrogen, prompting the use of the helium measurement method. The total span in production rate ratio is 1.58×10^{-8} to 1.06×10^{-7} in quartz and 1.02×10^{-8} to 7.89×10^{-8} in barium tungstate. At a given energy the production rates are higher in quartz than barium tungstate. All of these observations are in accord with predictions outlined in Section 1.2.

3.2. Neon, helium, uranium, and thorium in Durango fluorapatite

Three sets of experiments were done on splits of the Durango fluorapatite sample. In the first and third sets helium and neon were measured by peak height comparison while in the second set helium was measured by peak height comparison but neon was measured by isotope dilution (Tables 2 and 3). We used the measured ^{21}Ne/^{22}Ne ratio in the unspiked data set for the isotope dilution calculations (Table 2). These samples used our improved isotope dilution apparatus. All neon measurements are shown together in Fig. 4. Finally, Table 4 shows uranium and thorium measurements made by solution ICP-MS using isotope dilution

on splits of the same crushed sample of Durango fluorapatite following the procedures outlined in House and Farley (2000), and Table 5 shows (U–Th)/He age determinations on a subset of samples measured with a larger helium split for increased accuracy. Because of the significant correction for nucleogenic ^{22}Ne in fluorine-rich Durango fluorapatite, we observed no improvement in precision by switching to isotope dilution.

4. DISCUSSION

4.1. Comparison with predicted production rates

We observed good agreement (typically $< 3\%$ difference) between measured ^{21}Ne/^{4}He production rate ratios and the values predicted from the cross section data compiled in Gautheron et al. (2006) for quartz and barium tungstate. In contrast, we observed poor agreement when using Leya and Wieler's (1999) values (up to $\sim 10\%$ difference). The agreement for both analyzed phases indicates that the stopping powers and ^{18}O(α,n)^{21}Ne cross sections are both accurate at the level of better than 3%. If the stopping powers were incorrect, one or both phases would exhibit ^{21}Ne production rates inconsistent with predicted values, and the difference would not be systematic. If the cross section were incorrect, we would observe a systematic difference between measured and predicted production rates in each target regardless of stopping power.

The quartz data differ by an average of 2.8% from the modeled production rates, with the modeled rates slightly higher. The barium tungstate data differ by 0.6% with the
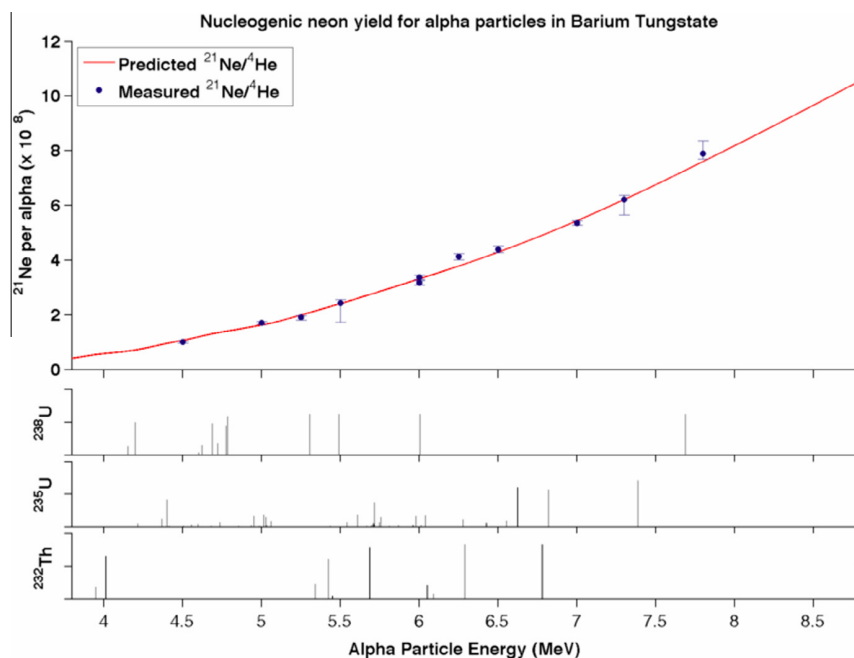

Fig. 3. Comparison of measured ^{21}Ne yields per alpha particle in barium tungstate compared with predictions based on the published cross sections of Gautheron et al. (2006) and stopping powers described in Section 1.2. Also shown are the relative distributions of alpha particle energies in each of the uranium and thorium decay chains.

Table 2
Neon isotope data of Durango fluorapatite. SE – standard error of the mean. Uncertainties on individual analyses reflect 1σ analytical error, while population uncertainties reflect 2σ standard error. When isotope dilution is used, ^{21}Ne concentrations calculated with isotope dilution (ID) and without are shown for comparison.

Number	Mass (mg)	^{21}Ne (Mat/g)	^{21}Ne ± (Mat/g)	^{21}Ne ± (%)	^{22}Ne (Mat/g)	^{22}Ne ± (Mat/g)	^{22}Ne ± (%)	^{22}Ne/^{21}Ne	^{22}Ne/^{21}Ne ±	^{22}Ne/^{21}Ne ± (%)
1	77.32	242	5	2.0	5165	45	0.87	21.3	0.6	2.6
2	75.04	239	5	1.9	5153	44	0.85	21.6	0.6	2.6
3	73.51	244	5	1.9	5228	44	0.85	21.4	0.5	2.5
4	87.05	249	5	1.9	5321	44	0.83	21.4	0.5	2.5
5	84.85	247	5	1.9	5303	44	0.83	21.5	0.5	2.5
6	88.77	244	5	1.8	5307	43	0.81	21.8	0.5	2.4
7	92.58	245	5	1.9	5296	43	0.82	21.7	0.5	2.5
8	110.9	247	5	1.9	5328	44	0.82	21.6	0.5	2.4
Average 1–8		244			5262			21.5		
SE (2σ)		0.88%			0.95%			0.46%		

Number	Mass (mg)	^{21}Ne (Mat/g)	^{21}Ne ± (Mat/g)	^{21}Ne ± (%)	^{21}Ne (Mat/g) ID	^{21}Ne ± (Mat/g) ID	^{21}Ne ± (%) ID
9	97.27	244	4	1.8	241	6	2.3
10	78.66	246	5	1.8	246	6	2.4
11	108.95	243	4	1.8	240	5	2.3
12	95.51	249	4	1.8	246	6	2.3
13	86.36	243	4	1.8	245	6	2.3
14	91.82	248	4	1.8	248	6	2.3
15	109.39	245	4	1.8	243	6	2.3
16	108.22	244	4	1.8	243	6	2.3
Average 9–16		245.25			244.01		
SE (2σ)		0.63%			0.80%		

Number	Mass (mg)	^{21}Ne (Mat/g)	^{21}Ne ± (Mat/g)	^{21}Ne ± (%)	^{22}Ne (Mat/g)	^{22}Ne ± (Mat/g)	^{22}Ne ± (%)	^{22}Ne/^{21}Ne	^{22}Ne/^{21}Ne ±	^{22}Ne/^{21}Ne ± (%)
17	90.0	255	1	1.6	5646	6	0.3	22.13	0.12	1.63
18	203	259	1	1.1	5793	4	0.2	22.33	0.08	1.09
19	26.1	242	2	3.0	5286	12	0.7	21.84	0.22	3.01
20	806	262	1	0.5	5732	2	0.1	21.86	0.04	0.55
21	28.2	238	2	2.9	5252	11	0.6	22.05	0.21	2.91
22	161	251	1	1.2	5711	5	0.3	22.77	0.09	1.24
23	237	258	1	1.0	5742	4	0.2	22.30	0.08	1.01
24	139	252	6	6.7	5507	21	1.1	21.89	0.50	6.79
25	479	250	4	5.2	5554	16	0.9	22.24	0.39	5.27
Average 17–25		252			5580			22.16		
SE (2σ)		2.1%			2.4%			0.9%		

modeled rates slightly lower. These relationships may imply that the cross section is correct and that the quartz stopping powers are 3.0% too low, but the standard deviation of the measured to modeled production rate ratios is about 4% for both targets, so the difference for both is within the uncertainty of the measurements.

4.2. Durango fluorapatite systematics

We find that the (U–Th)/^{21}Ne age of the Durango fluorapatite is 34.5 ± 3.3 Ma. This is in agreement with the accepted age of the standard (31.44 ± 0.18 Ma; McDowell et al., 2005), albeit with an uncertainty larger than we believe to be obtainable with the (U–Th)/^{21}Ne system, for reasons outlined below. For several of the third set of Durango fluorapatite measurements, we simultaneously measured (U–Th)/He ages of the same aliquots and obtained a mean age of 32.6 ± 0.7 Ma (Table 5). This value is near

the accepted age, and serves primarily as a check on the procedures used for noble gas and uranium and thorium analyses.

The three sets of Durango fluorapatite experiments reported here varied in methodology. The first two sets each contained eight samples of roughly the same mass, with the only difference being the use of isotope dilution for the second set of samples. The third set contained six samples of broadly varying mass chosen to explore the source of the unexpectedly high (U–Th)/^{21}Ne ages of the first two sets. The third set of analyses was made without isotope dilution, a necessary first step in analyzing fluorapatite samples because of the presence of natural ^{22}Ne. In the third set, it is clear that the ratio of measured neon signal to neon concentration in the mass spectrometer varies with sample size (Fig. 4), and that only the smallest samples provide ages close to the accepted age of the Durango fluorapatite standard. The

Table 3
Helium and Ne/He data for Durango fluorapatite. Uncertainties on individual analyses reflect 1σ analytical error, while population uncertainties reflect 2σ standard error.

Number	Mass (mg)	^{4}He (Tat/g)	^{4}He ± (Tat/g)	^{4}He ± (%)	^{21}Ne/^{4}He (10^{-8})	^{21}Ne/^{4}He (10^{-8}) ±	^{22}Ne/^{4}He (10^{-8})	^{22}Ne/^{4}He (10^{-8}) ±
1	77.32	5499	55	1	4.40	0.10	93.9	1.3
2	75.04	5518	55	1	4.33	0.09	93.4	0.9
3	73.51	5550	56	1	4.40	0.09	94.2	0.9
4	87.05	5578	56	1	4.46	0.10	95.4	0.9
5	84.85	5519	55	1	4.47	0.10	96.1	0.9
6	88.77	5566	56	1	4.38	0.09	95.3	0.9
7	92.58	5539	55	1	4.41	0.09	95.6	0.9
8	110.9	5561	56	1	4.44	0.09	95.8	0.9
Average 1–8		5541			4.41		95.0	
SE (2σ)		0.35%			1%		1%	

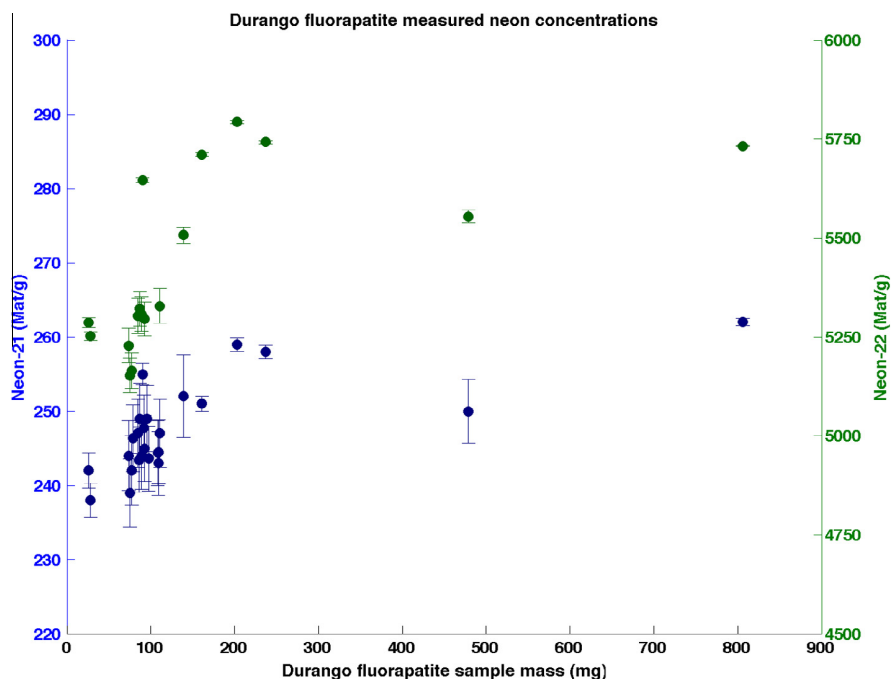| Number	Mass (mg)	^{4}He (Tat/g)	^{4}He ± (Tat/g)	^{4}He ± (%)	^{21}Ne/^{4}He (10^{-8})	^{21}Ne/^{4}He (10^{-8}) ±	^{21}Ne (ID)/^{4}He (10^{-8})	^{21}Ne (ID)/^{4}He (10^{-8}) ±
9	97.3	5550	56	1	4.39	0.09	4.34	0.11
10	78.7	5512	55	1	4.47	0.09	4.46	0.11
11	109.0	5494	55	1	4.42	0.09	4.37	0.11
12	95.5	5583	56	1	4.46	0.09	4.41	0.11
13	86.4	5503	55	1	4.42	0.09	4.44	0.11
14	91.8	5536	55	1	4.47	0.09	4.48	0.11
15	109.4	5563	56	1	4.40	0.09	4.36	0.11
16	108	5515	55	1	4.43	0.09	4.41	0.11
Average 9–16		5532			4.43		4.41	
SE (2σ)		0.40%			0.52%		0.81%	

Fig. 4. Durango fluorapatite ^{21}Ne (left axis) and ^{22}Ne (right axis) concentrations per gram of sample for all measured aliquots, plotted against sample size.

cause of this correlation is not clear, and is under investigation, but it may be related to ion source effects from incomplete removal of helium (prior to cryogenic separation, helium is present at a concentration approximately eight orders of magnitude higher than that of neon), or to other gases extracted from fluorapatite at high

Table 4
Uranium, thorium, and (U–Th)/Ne age data for Durango fluorapatite based on multiple aliquots for uranium and thorium and the population averages for neon for the first two datasets. Uncertainties on individual analyses reflect 1σ analytical error, while population uncertainties reflect 2σ standard error.

Sample	Mass (μg)	U (ppm)	U ± (ppm)	Th (ppm)	Th ± (ppm)	Th/U	Ne Age (Ma)	Ne Age ± (Ma)
A	133.6	9.21	0.12	173.9	1.2	18.8	33.8	1.4
B	257.3	8.99	0.13	169.8	1.1	18.9	34.6	1.4
C	298.2	8.87	0.15	170.2	1.2	19.2	34.7	1.4
D	100.9	8.79	0.13	167.4	1.0	19.0	35.3	1.4
Average A-D		8.97	0.18	170	2.7	19.0	34.6	2.4
E	27.37	9.51	0.11	183.7	0.6	19.3	32.5	1.3
F	29.54	9.33	0.10	173.3	0.6	18.6	35.1	1.4
G	39.33	9.20	0.06	175.2	0.6	19.0	35.2	1.4
H	35.57	9.20	0.08	176.0	0.6	19.1	35.1	1.4
I	35.12	9.38	0.08	178.1	0.6	19.0	34.0	1.4
Average E-I		9.32	0.13	177.3	4.0	19.0	34.4	2.1

Table 5
Helium and (U–Th)/He age data for part of the third dataset, using population averages of uranium and thorium. For these analyses, we increased the split size of the helium in order to obtain accurate (U–Th)/He ages.

Number	Mass (mg)	^{4}He (Tat/g)	^{4}He ± (Tat/g)	^{4}He ± (%)	He Age (Ma)	He Age ± (Ma)
5	28.23	5441	54	1	32.62	0.49
6	161.18	5435	54	1	32.58	0.49
7	236.62	5500	55	1	32.98	0.50

temperature. We note that for samples without nucleogenic ^{22}Ne, isotope dilution offers a path around such problems.

Apatite (U–Th)/^{22}Ne chronometry depends on the concentration of fluorine in the apatite, which is much more variable than the oxygen content. However, the production rate of ^{22}Ne is much higher than that of ^{21}Ne because while the cross section for ^{19}F(α,n)^{22}Ne is about half that of ^{18}O(α,n)^{21}Ne, the isotope abundance of ^{19}F (100%) is much higher than that of ^{18}O (∼0.2%). For example, we measure a ^{22}Ne/^{21}Ne production rate ratio of 21.52 ± 0.14 in Durango fluorapatite despite the fact that the F/O ratio is approximately 0.09. The exact relationship between F/O and ^{22}Ne/^{21}Ne production will vary slightly with oxygen isotope composition, sample age, and Th/U ratio, but will be approximately (^{22}Ne/^{21}Ne)/(F/O) = 0.0042 in near-end-member fluorapatite.

In addition to its use as a chronometer, (U–Th)/^{22}Ne may be combined with (U–Th)/^{21}Ne in the same mineral as a method for determining the fluorine content. If isotope dilution with ^{22}Ne is not used, ^{22}Ne can also be measured to investigate contamination with apatite or another fluorine-containing phase (e.g., titanite or fluorite).

4.3. Neon production rates in other uranium- and thorium-bearing minerals based on validated cross section

The appendix includes MATLAB code that can be used to compute nucleogenic neon production rates and (U–Th)/Ne ages for a variety of minerals. Users may define the uranium, thorium, helium, and neon contents and δ^{18}O of minerals. The user can also change the cross section, stopping power, mineral stoichiometries, and oxygen contents within

the code. This software has not been evaluated by *Geochimica et Cosmochimica Acta* or its reviewers.

In Table 6 we provide mineral-specific production rates of ^{21}Ne and ^{22}Ne per alpha particle for the decay chains starting with ^{238}U, ^{235}U, and ^{232}Th assuming secular equilibrium. These production rates can be used to calculate (U–Th)/Ne ages or to interpret neon/helium ratios in these minerals. Production rates average around 4.5×10^{-8} per alpha particle for ^{21}Ne for all three decay chains in each mineral. Using this value and assuming a Th/U ratio of 1, we estimate the age and uranium and thorium concentrations required to obtain measurable ^{21}Ne in a mineral (Fig. 5). In order to plot this result in two dimensions, we use "equivalent uranium" (alpha activity represented as concentration of uranium; Gastil et al., 1967) and define "measurable neon" as 65,000 atoms, or about 1.5 cps on our mass spectrometer. This requirement assumes a very low amount of non-nucleogenic ^{21}Ne; if a large air correction is required for an analysis, more nucleogenic neon is required to achieve good precision (Section 2.3.2).

4.3.1. Zircon, xenotime, thorite, and coffinite

The isostructural tetragonal minerals zircon and xenotime are commonly used for (U–Th)/Pb and, in the case of zircon, (U–Th)/He geochronometry and thermochronometry and may also be of interest for (U–h)/Ne chronometry. Based on comparison with ages of other thermochronometers, Gautheron et al. (2006) estimated a neon closure temperature in zircon of 400 ± 50 °C. Closure temperatures for the (U–Th)/Ne system intermediate between the helium and lead systems in these minerals raise the possibility of adding it to multiple chronometer thermochronology studies, and the (U–Th)/Ne system may also be

Table 6
Average ^{21}Ne and ^{22}Ne production rates calculated based on verified production rates in a variety of minerals for each decay chain for stoichiometric compositions (obtained at webmineral.com) and $\delta^{18}O = +6‰$. Production rates assume secular equilibrium for each decay chain.

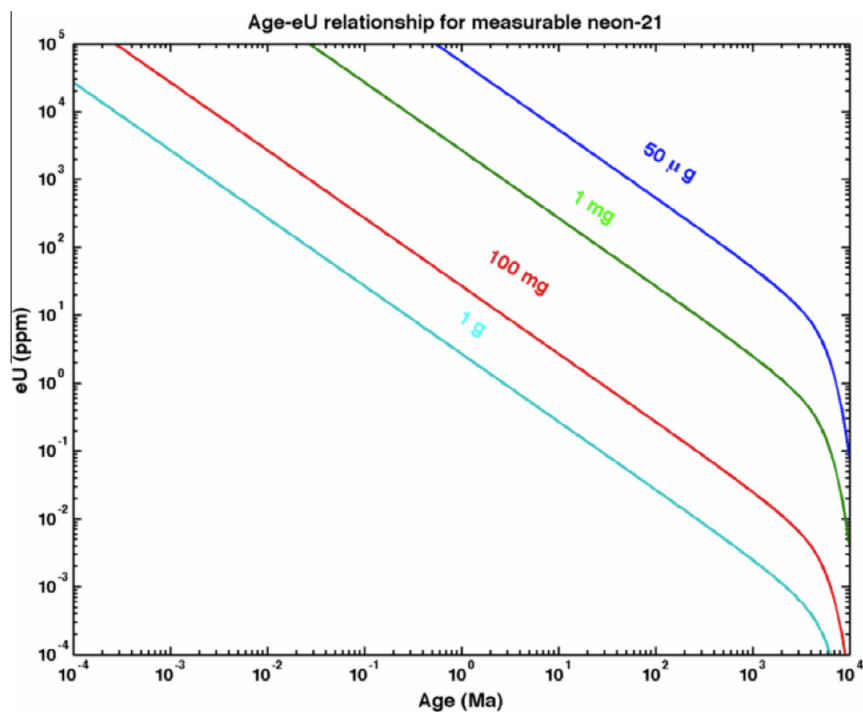| Mineral	Target Composition		Production rates for each decay chain from $^{18}O^*$			Production rates for each decay chain from $^{19}F^*$		
	[O]	[F]	^{238}U $^{21}Ne/^4He$	^{235}U $^{21}Ne/^4He$	^{232}Th $^{21}Ne/^4He$	^{238}U $^{22}Ne/^4He$	^{235}U $^{22}Ne/^4He$	^{232}Th $^{22}Ne/^4He$
	(wt fraction)	(wt fraction)	(10^{-8})	(10^{-8})	(10^{-8})	(10^{-8})	(10^{-8})	(10^{-8})
Quartz	0.5326	0	4.04	5.62	6.08	–	–	–
Barium Tungstate	0.1662	0	2.44	3.39	3.66	–	–	–
Zircon	0.3491	0	3.38	4.70	5.08	–	–	–
Xenotime-(Y)	0.3480	0	3.34	4.65	5.03	–	–	–
Thorite	0.1974	0				–	–	–
Coffinite	0.1953	0	2.85	3.95	4.26	–	–	–
Titanite	0.4080	0	3.33	4.63	5.01	–	–	–
Baddeleyite	0.2597	0	2.90	4.04	4.36	–	–	–
Hematite	0.3006	0	2.80	3.89	4.21	–	–	–
Maghemite	0.3006	0	2.80	3.89	4.21	–	–	–
Goethite	0.3602	0	3.14	4.37	4.73	–	–	–
Magnetite	0.2764	0	2.60	3.62	3.91	–	–	–
Calcite	0.4795	0	3.59	5.00	5.41	–	–	–
Aragonite	0.4795	0	3.59	5.00	5.41	–	–	–
Uraninite	0.1185	0	2.17	3.01	3.24	–	–	–
Thorianite	0.1212	0				–	–	–
Cryptomelane	0.3485	0	3.14	4.37	4.72	–	–	–
Fluorapatite	0.3801	0.0352	3.02	4.20	4.54	42.1	64.5	73.9
Fluorite	0	0.4867	–	–	–	595	915	1044

Fig. 5. Relationship between age and effective uranium concentration (eU = U + 0.235 × Th, accounting for alpha dose over time) required for a measurable amount of ^{21}Ne (defined as 65,000 atoms) in a generic mineral with a fixed $^{21}Ne/^4He$ production rate ratio of 4.5 × 10^{-8}, assuming a Th/U ratio of 1. The different lines reflect different sample sizes. The actual production rate will vary slightly according to mineralogy and Th/U ratio.

used as a tool to expose or investigate problems with these chronometers in low-temperature and volcanic systems. Thorite and coffinite are less common, especially as euhedral crystals suitable for chronological studies, but may occur as inclusions or associated accessories in other minerals of chronological interest, and may be of interest themselves in unusual settings.

4.3.2. Titanite and baddeleyite

Other common candidates for (U–Th)/Pb dating include titanite and baddeleyite, both of which may be targeted for (U–Th)/Ne dating for the same reasons as the silicates in Section 4.3.1. Replacement reactions between baddeleyite and zircon may be more likely to completely reset the (U–Th)/Ne system than the (U–Th)/Pb system, especially when the reaction occurs in the direction zircon to baddeleyite, because lead is very resistant to diffusive loss (Cherniak and Watson, 2001). The different production rates of neon in zircon and baddeleyite, arising from differences in oxygen concentration, should also be noted because they often occur in close association.

4.3.3. Uraninite, thorianite, and the implications of micro-inclusions

Minerals such as uraninite and thorianite are unlikely to occur in large crystals with well behaved (U–Th)/Ne systematics, but may occur as micro-inclusions in other minerals of interest, especially as alteration products in hydrothermal systems. Even very small inclusions will have a profound impact on the (U–Th)/Ne systematics of host phases due to the very high uranium and thorium concentrations of these minerals and the fact that neon production peaks very close to the source of alpha particles. Furthermore, very uranium-rich phases will become radiation damaged and will probably exhibit anomalous diffusivities for neon, as is observed in similar situations for helium (Hurley, 1954; Nasdala et al., 2004; Shuster et al., 2006; Shuster and Farley, 2009; Guenthner et al., 2013).

The phases above are typically very high in uranium and/or thorium, and will therefore likely exhibit high nucleogenic ^{21}Ne concentrations relative to air contamination and small amounts of cosmogenic contamination. The phases below typically have much lower uranium and thorium concentrations, so air contamination in the vacuum line and air adsorbed to and trapped within the samples will be a more significant factor affecting the precision of the measurements, and samples must be more carefully selected and screened for cosmogenic neon contamination. This applies especially to samples that form at or near the Earth's surface, such as carbonates, where cosmogenic neon contamination is more likely.

4.3.4. Hematite, goethite, and magnetite

Iron oxides frequently contain ppm-level concentrations of uranium and thorium that are adequate for the production of radiogenic helium and neon (Lippolt et al., 1993; Shuster et al., 2005; Farley and Flowers, 2012). These uranium and thorium concentrations and high common lead concentrations prevent the use of the (U–Th)/Pb system on these minerals. Neon appears to be retained at surface temperatures in iron oxides, and the (U–Th)/Ne system is therefore already in use as a geochronometer in hematite (Farley and Flowers, 2012). Because of the low uranium and thorium concentrations in the minerals themselves, care must be taken to either exclude or account for inclusions of other minerals that contain these elements.

4.3.5. Calcite and aragonite

Carbonates are similar to iron oxides in that low uranium and thorium concentrations and common lead contamination sometimes complicate the (U–Th)/Pb system (Rasbury and Cole, 2009) while low and variable helium retention complicates the (U–Th)/He system (Cros et al., 2014). Neon production rates are insufficient for dating of most Pleistocene marine carbonates using the (U–Th)/Ne system due to low uranium and thorium concentrations, but older deposits or deposits with unusually high uranium and thorium concentrations are candidates for (U–Th)/Ne geochronology.

5. CONCLUSIONS

We present direct measurements of the ^{21}Ne production rates of mono-energetic alpha particles in two targets, which allows us to verify the ^{18}O(α,n)^{21}Ne cross section and the stopping powers independently. These measurements agree well with the cross section data compiled by Gautheron et al. (2006) and with stopping power calculations using SRIM, affirming the validity of the calculated production rates at the ~3% level. These production rates are presented here along with software for the calculation of production rates in other minerals and of (U–Th)/Ne ages. These results allow geochemists to apply the (U–Th)/Ne system to questions about Earth history, including medium-temperature thermochronometry and geochronometry in rocks with high uranium or older than ~10 Ma, with a better understanding of the inherent uncertainty in the system.

APPENDIX A. SUPPLEMENTARY DATA

The software used to model neon production rates and to calculate neon ages is included and is also freely available at www.gps.caltech.edu/~scox/neon_age_calc.

Supplementary data associated with this article can be found, in the online version, at http://dx.doi.org/10.1016/j.gca.2014.08.036.

REFERENCES

Bair J. and Willard H. (1962) Level structure in Ne^{22} and Si^{30} from the reactions $O^{18}(\alpha, n)Ne^{21}$ and $Mg^{26}(\alpha, n)Si^{29}$. *Phys. Rev.* **128**, 299–304.

Bair J. K. and Del Campo J. G. (1979) Neutron yields from alpha-particle bombardment. *Nucl. Sci. Eng.* **71**, 18–28.

Behrens H. (2010) Noble Gas Diffusion in Silicate Glasses and Melts. *Rev. Mineral. Geochem.* **72**, 227–267.

Boyce J. and Hodges K. V. (2005) U and Th zoning in Cerro de Mercado (Durango, Mexico) fluorapatite: insights regarding the impact of recoil redistribution of radiogenic ^{4}He on (U–Th)/He thermochronology. *Chem. Geol.* **219**, 261–274.

Cherniak D. J. and Watson E. B. (2001) Pb diffusion in zircon. *Chem. Geol.* **172**, 5–24.

Cherniak D. J., Thomas J. B. and Watson E. B. (2014) Neon diffusion in olivine and quartz. *Chem. Geol.* **371**, 68–82.

Cros A., Gautheron C., Pagel M., Berthet P., Tassan-Got L., Douville E., Pinna-Jamme R. and Sarda P. (2014) ^{4}He behavior in calcite filling viewed by (U–Th)/He dating, ^{4}He diffusion and crystallographic studies. *Geochim. Cosmochim. Acta* **125**, 414–432.

Eiler J. M., Crawford A., Elliott T., Farley K. A., Valley J. W. and Stolper E. M. (2000) Oxygen isotope geochemistry of oceanic-arc lavas. *J. Petrol.* **41**, 229–256.

Farley K. (2000) Helium diffusion from apatite: general behavior as illustrated by durango fluorapatite. *J. Geophys. Res.* **105**, 2903–2914.

Farley K. A. and Flowers R. M. (2012) (U–Th)/Ne and multidomain (U–Th)/He systematics of a hydrothermal hematite from eastern Grand Canyon. *Earth Planet. Sci. Lett.* **359–360**, 131–140.

Gastil R. G., DeLisle M. and Morgan J. R. (1967) Some effects of progressive metamorphism on zircons. *Geol. Soc. Am. Bull.* **78**, 879.

Gautheron C., Tassan-Got L. and Farley K. (2006) (U–Th)/Ne chronometry. *Earth Planet. Sci. Lett.* **243**, 520–535.

Guenthner W. R., Reiners P. W., Ketcham R. A., Nasdala L. and Giester G. (2013) Helium diffusion in natural zircon: radiation damage, anisotropy, and the interpretation of zircon (U–Th)/He thermochronology. *Am. J. Sci.* **313**, 145–198.

Hansen L. F., Anderson J. D., McClure J. W., Pohl B. A., Stelts M. L., Wesolowski J. J. and Wong C. (1967) The (α, n) cross sections on ^{17}O and ^{18}O between 5 and 12.5 MeV. *Nucl. Phys. A: Nucl. Hadr. Phys.* **98**, 25–32.

House M. and Farley K. (2000) Helium chronometry of apatite and titanite using Nd-YAG laser heating. *Earth Planet. Sci. Lett.* **183**, 365–368.

Hurley P. M. (1954) The helium age method and the distribution and migration of helium in rocks. In *Nuclear Geology* (ed. H. Faul). Wiley and Sons. pp. 301–329.

Hünemohr H. (1989) Edelgase in U- und Th-reichen Mineralen und die Bestimmung der ^{21}Ne-Dicktarget-Ausbeute der ^{18}O$(\alpha \cdot n)^{21}$Ne- Kernreaktion im Bereich 4.0–8.8 MeV. Max-Planck-Institut fur Chemie.

Kennedy B. M., Hiyagon H. and Reynolds J. H. (1990) Crustal neon: a striking uniformity. *Earth Planet. Sci. Lett.* **98**, 277–286.

Kyser T. K. and Rison W. (1982) Systematics of rare gas isotopes in basic lavas and ultramafic xenoliths. *J. Geophys. Res.* **87**, 5611.

Leya I. and Wieler R. (1999) Nucleogenic production of Ne isotopes in Earth's crust and upper mantle induced by alpha particles from the decay of U and Th. *J. Geophys. Res.* **104**, 15439–15450.

Lippolt H. J., Wernicke R. S. and Boschmann W. (1993) ^{4}He diffusion in specular hematite. *Phys. Chem. Minerals* **20**, 415–418.

McDowell F. W., McIntosh W. C. and Farley K. A. (2005) A precise ^{40}Ar–^{39}Ar reference age for the Durango apatite (U–Th)/He and fission-track dating standard. *Chem. Geol.* **214**, 249–263.

Murata T., Matsunobu H. and Shibata K. (2006) Evaluation of the (α, xn) reaction data for JENDL/AN-2005. *Jpn. Atom. Energy Agency-Res.*, **78**.

Nadeau S. L., Epstein S. and Stolper E. (1999) Hydrogen and carbon abundances and isotopic ratios in apatite from alkaline intrusive complexes, with a focus on carbonatites. *Geochim. Cosmochim. Acta* **63**, 1837–1851.

Nasdala L., Reiners P. W., Garver J. I., Kennedy A. K., Stern R. A., Balan E. and Wirth R. (2004) Incomplete retention of radiation damage in zircon from Sri Lanka. *Am. Mineral.* **89**, 219–231.

Niedermann S. (2002) Cosmic-ray-produced noble gases in terrestrial rocks: dating tools for surface processes. *Rev. Mineral. Geochem.* **47**, 731–784.

Norman E., Chupp T., Lesko K., Grant P. and Woodruff G. (1984) ^{22}Na production cross sections from the ^{19}F(α, n) reaction. *Phys. Rev. C: Nucl. Phys.* **30**, 1339–1340.

Rasbury E. T. and Cole J. M. (2009) Directly dating geologic events: U–Pb dating of carbonates. *Rev. Geophys.* **47**, RG3001.

Shuster D. L. and Farley K. A. (2005) Diffusion kinetics of proton-induced ^{21}Ne, ^{3}He, and ^{4}He in quartz. *Geochim. Cosmochim. Acta* **69**, 2349–2359.

Shuster D. L. and Farley K. A. (2009) The influence of artificial radiation damage and thermal annealing on helium diffusion kinetics in apatite. *Geochim. Cosmochim. Acta* **73**, 183–196.

Shuster D. L., Flowers R. M. and Farley K. A. (2006) The influence of natural radiation damage on helium diffusion kinetics in apatite. *Earth Planet. Sci. Lett.* **249**, 148–161.

Shuster D. L., Vasconcelos P. M., Heim J. A. and Farley K. A. (2005) Weathering geochronology by (U–Th)/He dating of goethite. *Geochim. Cosmochim. Acta* **69**, 659–673.

Solé J. and Pi T. (2006) Determination of the ^{22}Ne$_{nucl}$/^{4}He$_{rad}$ ratio in natural uranium-rich fluorite by mass. *Phys. Rev. C: Nucl. Phys.* **74**, 047601.

Tournour C. C. and Shelby J. E. (2008a) Helium solubility in alkali silicate glasses and melts. *Phys. Chem. Glasses – Eur. J. Glass Sci. Technol. Part B* **49**, 207–215.

Tournour C. C. and Shelby J. E. (2008b) Neon solubility in silicate glasses and melts. *Phys. Chem. Glasses – Eur. J. Glass Sci. and Technol. Part B* **49**, 237–244.

Wetherill G. (1954) Variations in the isotopic abundances of neon and argon extracted from radioactive minerals. *Phys. Rev.* **96**, 679–683.

Wrean P. and Kavanagh R. (2000) Total cross sections and reaction rates for ^{19}F$(\alpha, n)^{22}$Na, ^{22}Ne$(p, n)^{22}$Na, and their inverses. *Phys. Rev. C: Nucl. Phys.* **62**, 055805.

Yatsevich I. and Honda M. (1997) Production of nucleogenic neon in the Earth from natural radioactive decay. *J. Geophys. Res.* **102**, 10291.

Ziegler J. F., Ziegler M. D. and Biersack J. P. (2010) SRIM – The stopping and range of ions in matter (2010). *Nucl. Instrum. Methods Phys. Res., Sect. B* **268**, 1818–1823.

Associate editor: Pete Burnard